Published in final edited form as:
IEEE Trans Biomed Eng. 2009 August ; 56(8): 2131–2139. doi:10.1109/TBME.2009.2021576.

Surface Current Density Mapping for Identification of Gastric Slow Wave Propagation

L. A. Bradshaw,
Member, IEEE, Departments of Surgery and Physics and Astronomy, Vanderbilt University and the Department of Physics, Lipscomb University, Nashville, TN 37235 USA (phone: 615-322-0705; fax: 615-322-4419; e-mail: alan.bradshaw@vanderbilt.edu)

L. K. Cheng,
Bioengineering Institute, University of Auckland, Auckland, New Zealand (e-mail: l.cheng@auckland.ac.nz)

W. O. Richards, and
Department of Surgery, Vanderbilt University, Nashville, TN 37235 USA (email: bill.richards@vanderbilt.edu)

A. J. Pullan
Department of Engineering Science and the Bioengineering Institute, University of Auckland, Auckland, New Zealand (email: a.pullan@auckland.ac.nz)

Abstract

The magnetogastrogram records clinically relevant parameters of the electrical slow wave of the stomach noninvasively. Besides slow wave frequency, gastric slow wave propagation velocity is a potentially useful clinical indicator of the state of health of gastric tissue, but it is a difficult parameter to determine from noninvasive bioelectric or biomagnetic measurements. We present a method for computing the surface current density (SCD) from multichannel magnetogastrogram recordings that allows computation of the propagation velocity of the gastric slow wave. A moving dipole source model with hypothetical as well as realistic biomagnetometer parameters demonstrates that while a relatively sparse array of magnetometer sensors is sufficient to compute a single average propagation velocity, more detailed information about spatial variations in propagation velocity requires higher density magnetometer arrays. Finally, the method is validated with simultaneous MGG and serosal EMG measurements in a porcine subject.

Index Terms

biomagnetism; current dipole; electrogastrogram; magnetogastrogram; SQUID magnetometer

I. Introduction

Gastric electrical activity controls the mixing and propulsion of foods in preparation for digestion and processing in the small and large bowel. A region of the proximal antrum along the greature curvature of the stomach generates a slow wave oscillating near 3 cycles per minute (cpm) that propagates quickly around the circumference of the stomach and more slowly down the stomach's longitudinal axis [1].

The gastric slow wave produces an extracellular potential that may be recorded with cutaneous abdominal electrodes [2–4]. Associated intracellular and extracellular current flow also produces a magnetic field which may be measured [5]. Previous studies in our laboratory have

shown that a Superconducting QUantum Interference Device (SQUID) magnetometer can identify the gastric and intestinal slow wave, the known frequency gradient of the GI tract and changes in slow wave frequency associated with abnormal conditions such as ischemia and uncoupling [6;7].

The identification of slow wave parameters from recordings of gastric electrical activity thus has clinical implications. The gastric slow wave frequency may be measured with cutaneous electrodes, but alternating low- and high-conductivity abdominal tissue layers smooth and attenuate electric potentials, frustrating the determination of other potentially useful diagnostic slow wave parameters such as propagation velocity [8–10]. Biomagnetic fields associated with the gastric slow wave are not as affected by tissue conductivities as the electric potential, and may thus facilitate a more complete characterization of clinically relevant spatiotemporal slow wave parameters. We present a computationally-efficient method for utilizing multichannel biomagnetic measurements of the gastric slow wave to characterize slow wave propagation and to determine the gastric slow wave propagation velocity noninvasively.

II. Methods

A. Gastric Biomagnetic Fields

The biomagnetic field is detected noninvasively with a SQUID biomagnetometer. Typically, these devices are configured in a gradiometric arrangement to subtract uniform ambient noise fields. Intracellular and extracellular currents produced by ion flows across membranes in electrically active tissue generate the extracorporeal magnetic fields. The biomagnetic induction field of a current source in a homogeneous medium is given by the law of Biot-Savart as

$$\mathbf{B}_0(\mathbf{r})=\frac{\mu_0}{4\pi}\int_{\Omega}\frac{\nabla\times\mathbf{J}^i(\mathbf{r}')}{|\mathbf{r}-\mathbf{r}'|}d\mathbf{r}', \tag{1}$$

where μ_0 is the magnetic permeability of free space, the impressed current density $\mathbf{J}^i$ is located at $\mathbf{r}'$ with the integration over the source volume Ω and the magnetic induction field $\mathbf{B}_0$ evaluated at $\mathbf{r}$. The magnetic field is also affected by inhomogeneities in the conductivity and geometry of the volume containing the current. To assess methods of analysis for biomagnetic data, we used both a horizontally layered volume conductor model and a piecewise-homogeneous boundary element model of a realistic abdomen. In these models, the biomagnetic induction is includes contributions from volume currents [11]

$$\mathbf{B}(\mathbf{r})=\mathbf{B}_0(\mathbf{r})-\frac{\mu_0}{4\pi}\sum_{j=1}^{n}\left(\sigma_j'-\sigma_j''\right)\int_{\mathbf{s}_j}V(\mathbf{r}')\mathbf{n}(\mathbf{r}')\times\frac{\mathbf{r}-\mathbf{r}'}{|\mathbf{r}-\mathbf{r}'|^3}d\mathbf{S}_j \tag{2}$$

where the volume conductor is divided into regions bounded by surface $\mathbf{S}_j$ and the summation is performed over all such surfaces. σ_j' and σ_j'' represent the conductivities on the inner and outer surfaces of $\mathbf{S}_j$, respectively, V is potential and $\mathbf{n}$ is a unit vector normal to the surface. In a horizontally-layered volume conductor with a bounding surface in the *xy* plane, equation (2) simplifies to [12]

$$\mathbf{B}(\mathbf{r})=\frac{\mu_0}{4\pi K^2}(\mathbf{Q}\times\mathbf{a}\cdot\hat{\mathbf{z}}\nabla K - K\hat{\mathbf{z}}\times\mathbf{Q}) \tag{3}$$

where $\mathbf{a} = \mathbf{r} - \mathbf{r}'$ is the distance between the source and field point, $K = a(a+\mathbf{a}\cdot\hat{\mathbf{z}})$, $\hat{\mathbf{z}}$ is a unit vector normal to the surface (along the z direction) and $\mathbf{Q}$ is a current dipole defined as

$$\mathbf{Q}=\int \mathbf{J}^i(\mathbf{r}')d\mathbf{r}'. \tag{4}$$

The electric potential on the gastric serosal surface assuming a homogeneous volume conductor is

$$V(\mathbf{r})=\frac{1}{4\pi\sigma}\int\frac{\nabla\cdot\mathbf{J}^i(\mathbf{r}')}{|\mathbf{r}-\mathbf{r}'|}d\mathbf{r}', \tag{5}$$

which is given by the dipole approximation as [12],

$$V(\mathbf{r})=\frac{1}{4\pi\sigma}\frac{\mathbf{Q}\cdot\mathbf{r}}{|\mathbf{r}-\mathbf{r}'|}.$$

1) Horizontally Layered Volume Conductor—Using these equations, we computed the magnetogastrogram (MGG) recorded in SQUID detectors 2 cm above the abdominal surface, which was modeled as a homogeneous conducting half-space. We computed the fields from this model both in a hypothetical 176 channel SQUID system and in an array corresponding to the Tristan 637i biomagnetometer currently in use at Vanderbilt's Gastrointestinal SQUID Technology Laboratory. The high-density 176 channel biomagnetometer consisted of gradiometer detectors arranged in a rectangular 16×11 pattern with the sensors separated by 2 cm, as in Figure 1.

2) Realistic Volume Conductor—We further extended the simple horizontally layered model to the case of a piecewise-homogeneous realistic geometry. This realistic volume conductor model, shown in Figure 2 was a boundary element surface model with bi-cubic Hermite basis function interpolation constructed from the visible human project anatomical images [13–15]. We calculated the magnetic field of primary sources in free space as well as the electric potential on the torso surface by solving a generalized Laplace's equation. We then integrated around the boundary of the torso to calculate the magnetic field due to the volume conductor (secondary) sources. Finally, we evaluated the full magnetic field in the z direction at the 176 sensor locations and subjected this field to the SCD procedure.

B. Propagating Dipole Source Model

The gastric slow wave originates along the greater curvature of the stomach and propagates quickly circumferentially around the body of the stomach [16;17]. It propagates more slowly longitudinally down the stomach [1;18;19]. To simulate gastric propagation, we used a ring of 20 current dipoles 4 cm in diameter centered 3 cm below the surface of the abdomen. The dipoles in the ring were oriented tangential to the volume conductor surface along the $-x$ direction and propagated horizontally across a 10 cm distance, as shown in Figure 1, to represent longitudinal aborad propagation of the slow wave. The longitudinal propagation

velocity increases distally, which we simulated by setting the propagation velocity to 2.5 mm/s at the pacemaker location with a stepwise increase of 2.5 mm/s every 2.5 cm.

1) Surface Current Density Calculation—The surface current density (SCD) method was first proposed by Hosaka and Cohen (the H-C Transformation) [20–23] and is computed essentially by taking the curl of the measured magnetic field,

$$\tilde{\mathbf{J}} = \frac{1}{\mu_0} \nabla \times \mathbf{B}, \tag{7}$$

where the vector $\tilde{\mathbf{J}}$ represents the surface current density. This quantity is a vector and so different components of the surface current density can be obtained. In most biomagnetic situations, an array of sensors records the *z* component of the magnetic field (defined as in Figure 1). The array of magnetic field measurements at different spatial points is essential to the computation of the surface current density as the curl operation requires the existence of spatial derivatives of the magnetic field. In the case of an array of measurements of B_z made in the *x*-*y* plane, the two components of the surface current density are

$$\tilde{J}_x = \frac{1}{\mu_0} \left(\frac{\partial B_z}{\partial y} - \frac{\partial B_y}{\partial z} \right), \text{and} \tag{8}$$

$$\tilde{J}_y = -\frac{1}{\mu_0} \left(\frac{\partial B_z}{\partial x} - \frac{\partial B_x}{\partial z} \right) \tag{9}$$

In a standard biomagnetic measurement situation, the terms containing contributions from the spatial derivatives of the tangential field components B_x and B_y are not usually available, and have been neglected in the estimation of the SCD in this case.

Maxwell's equations are valid pointwise, so the SCD, which estimates the field differences at measurement locations rather than at source locations, does not represent a real current density [24]. Clearly, there exists no current density at the location of the measurement and thus, the curl of the magnetic field at this location is also zero. Nevertheless, the nonzero values obtained by the H-C transformation were related by Hosaka and Cohen to current running just under the surface parallel to the measurement plane.

In a realistic measurement situation, the curl is estimated by spatial differences in the magnetic field measured at distinct spatial locations. With two separate components of the surface current density computed from these curl calculations, visualization can consist of a map of arrows representing the *x*- and *y* components of the surface current density. Alternatively, the magnitude of the SCD can be computed and presented as a two-dimensional map. For sequential temporal samples, these maps can be animated to allow spatiotemporal assessment of data. For purposes of presentation in this manuscript, we present SCD sequences as frames of contour plots with time running from the top to the bottom of the figure. The magnetic field values sampled at specific locations are interpolated using triangle-based linear interpolation for a potentially more accurate SCD estimate.

C. Experimental Protocol

To test the method in an experimental situation, we performed laparotomy on nine adult male anesthetized pigs and attached an electrode platform to a region in the terminal antrum of the gastric serosa. Procedures were approved by Vanderbilt's Institutional Animal Care and Use Committee. The serosal electrode platform contained 12 bipolar platinum electrodes arranged in a 4×3 grid. Electrode pairs were separated by a distance of 0.5 cm with a bipolar baseline of 0.2 cm. We connected the electrodes to an optically isolated amplifier (James Long Co., New York) operating on DC power that could be used inside a magnetically shielded room.

The animal was placed underneath a SQUID biomagnetometer (Model 637i, Tristan Technologies, San Diego, CA) for simultaneous recording of serosal potential and the transabdominal magnetogastrogram. The Tristan 637i contains 19 detector coils located at the bottom of liquid helium filled dewar arranged in a close-packed honeycomb array. These 19 coils detect the *z* component of the magnetic field. The 637i also contains five vector sensors, four located on the periphery and one in the center of the array, but these were not used in the computation of the SCD. We used LabVIEW (National Instruments, Austin, TX) to acquire data at 3 kHz and later downsampled to 300 Hz for postprocessing. The high sample rate is necessitated by the SQUID amplifier instrumentation employed (Model 5000, Quantum Dynamics, San Diego, CA). These data were loaded into MATLAB (Mathworks, Natick MA) and scaled to units of pT using previously-determined calibration factors for the 637i. To compute the SCD we filtered SQUID data digitally using a narrow bandwidth (2–10 cpm) to reduce contributions from all non-gastric signal sources and employed the algorithm as explained above. We employed a standard cubic spline interpolation of the 19 sensor locations onto a 21 × 21 grid of points spanning 20 cm in the *x* and *y* directions with a spacing of 1.0 mm between points. We also investigated the improvement in the SCD estimate with a factor of two increase in interpolation to a spacing of 0.5 mm.

III. Results

A. Horizontally Layered Volume Conductor

Serosal electric potentials computed just outside the simulated gastric surface reflect the propagating current dipole ring. We found that the near-field signature is nearly identical to that of a single propagating current dipole located 3 cm below the cutaneous surface (at the center of the dipole ring), as shown in Figure 1, which suggests that a single dipole source model is sufficient. Potentials computed from equation (5) just outside the propagation path are shown at progressively distal electrodes from top to bottom in Figure 3. They demonstrate a bipolar waveform that propagates at the programmed rate and with the spatial velocity gradient from the corpus (x = +5.0 cm) to the terminal antrum/pylorus (x = −5.0 cm) over 20 seconds. The pattern resets to the proximal antrum every 20 seconds, reflecting the 3 cycle per minute rhythm of the gastric slow wave moving dipoles.

Magnetic fields computed in the simulated 176 channel SQUID array (Figure 4a) also exhibit propagation of the source dipoles. In this ideal, noiseless situation, the pattern maxima (or minima) could be tracked for an accurate assessment of slow wave propagation and a reliable estimate of propagation velocity. However, the field patterns are the double lobes that characterize current dipoles, and thus, the maxima and minima are displaced laterally from the actual dipole position.

The surface current density (SCD) maps computed from the magnetic field data have a single peak that is located at the position of the current dipole (Figure 5). Tracking this SCD maximum over time allows calculation of the propagation velocity, as shown in Figure 6a. The propagation velocity computed by taking the slope of the plot of SCD maximum vs. time

correctly reflected the increasing slow wave velocity. As Figure 5a demonstrates, successive patterns exhibit maxima that move across the detector array faster in the terminal antrum than in the corpus. As the velocity is estimated by the slope of the SCD maximum line, multiple velocities can be estimated by linear fits over smaller time intervals. Using this method, we computed the propagation velocity over one-quarter, one-half and one full slow wave cycle. Table I summarizes the results. The SCD method is capable of accurately reproducing the dipole propagation velocity. If an entire slow wave cycle is used, the estimated propagation velocity is equal to the average of the actual propagation velocity. Dividing the slow wave cycle in half shows that the slow wave propagates faster in the second half of the cycle. The stepwise acceleration of the propagation is accurately reproduced when the slow wave cycle is divided in fourths.

B. Realistic Volume Conductor Model

When we repeated this simulation using a realistic torso volume conductor model, we obtained similar results. Figure 5b shows the SCD sequence from magnetic fields in the realistic torso model. Differences in the field introduced by the more complex abdominal volume conductor geometry were minimal and did not prevent us from identifying clear propagation in the SCD pattern. The SCD pattern maxima tracked almost identical to the conducting half-space model. The resulting propagation velocity profile reflected the spatial velocity gradient, as with the homogeneous half-space model.

C. Tristan 637i Biomagnetometer, Sources Centered

To test the ability of the SCD method in a more realistic situation, we repeated the simulation with the actual SQUID parameters used in the 637i biomagnetometer in the VU-GIST lab. We expected diminished spatial frequency content in the signals because of the sparser sensor array in the 637i. The resulting magnetic fields are shown in Figure 4b. Figure 5c (solid line) shows that while propagation is still evident, the decrease in spatial frequency content causes the dipolar signal to appear stationary for several seconds and then to “jump” between sensors within a very short time interval.

This effect could lead one to believe that the propagating slow wave had momentarily stalled and then restarted at an accelerated rate. For this reason, any gradient in the propagation velocity is obscured. However, we still find that taking the average of the SCD’s maximal position change divided into the average time difference yields a velocity that reflects the average underlying slow wave propagation (see Table I). Nonetheless, with the known acceleration of slow wave propagation, the limited spatial resolution of the 637i magnetometer allows only an average estimate of propagation velocity and prevents the determination of the acceleration or the velocity gradient. Nevertheless, the estimated average propagation velocity agrees well with the average known velocity.

D. Tristan 637i Biomagnetometer, Eccentric Sources

We noted that with the line of dipole propagation chosen to coincide with the *x*-axis and thus the middle row of magnetometer sensors, and with the dipole oriented along the negative *x* direction, there was no magnetic field in the sensors directly above the propagating current dipoles, a situation unlikely to occur in normal experimental or clinical circumstances (Figure 4b). To investigate the amount of information that was lost by this coincidence of current propagation and sensors, we recomputed the magnetic field with all parameters the same as before, except with the current propagating along $y = -1$ cm instead of along the *x*-axis. Figure 4c shows the magnetic fields in the Tristan 637i from the off-center propagating current pattern. The SCD maps computed from the off-center propagation are shown in Figure 5d and the resulting position of the SCD maxima as a function of time is shown as the dashed line in Figure 6b. The additional information afforded by nonzero magnetic fields in the five middle

magnetometer sensors allows a much more sensitive estimation of SCD maxima position and thus a more accurate computation of the propagation velocity. Doubling the interpolation of magnetic field values results in a modest improvement of estimated source location (and hence propagation velocity).

E. Experimental Results

We also computed the propagation velocity of the SCD distribution obtained from experimental biomagnetic recordings in the porcine subjects. Figure 5e shows the SCD distribution as it evolves over 20 seconds. The pattern maxima moves from the subject's upper left side to the right, and the average SCD propagation velocity can be determined by tracking the maxima as before. We compared these SCD propagation velocities with the propagation velocity determined by direct measurement of time lag for signal features in adjacent serosal electrode recordings and show the results in Figure 7.

The propagation velocities determined from four antral electrodes were very similar since they were close in proximity to each other. The propagation velocity determined from the SCD maps also agreed well with serosal electrode recordings, although there is a statistically significant difference between the most proximally located serosal electrode and SCD propagation velocities ($p < 0.05$).

IV. Discussion

We used a simple current dipole model of the propagating gastric slow wave to demonstrate how the computation of the surface current density can be used with multichannel biomagnetic measurements to estimate the propagation velocity of the underlying electrical activity. By testing the source model in different measurement situations, we observed that while propagation is evident in the SCD, the spatial sampling provided by the magnetometer instrumentation is a critical parameter in the determination of propagation. A magnetometer array with a higher density was able to distinguish subtle spatial variations in the slow wave propagation velocity, but lower spatial sampling limits the ability of the SCD method to distinguish variations. It is possible that a different interpolation scheme than the linear method we used would also produce better results [25].

We showed that whereas the 19 channel Tristan 637i biomagnetometer currently used in our laboratory is sufficient to determine an average gastric slow wave propagation velocity, a higher rate of spatial sampling is required to detect the known spatial gradient in the propagation velocity. In both a piecewise homogeneous conductor and a realistic abdominal volume conductor, a higher density magnetometer array was able to better characterize the propagation velocity profile.

We further computed the SCD sequence from MGG data obtained from porcine subjects while simultaneous serosal electromyograms were measured. SCD maps from those data demonstrate clear propagation and tracking of the maxima allowed us to estimate the average propagation velocity. The propagation velocity determined from SCD pattern maxima agreed extremely well with that determined by direct measurements using serosal electrodes.

The computation of the surface current density in a measurement situation was accomplished by computing the difference in the *z* magnetic field component between adjacent magnetometer channels. Even if the magnetic field spatial differences could be computed exactly, the fact that they are measured at points distant from the actual physiological source of current implies that the SCD still does not exactly represent the underlying current distribution. Nevertheless, computation of the SCD can still reveal approximate information about biological current sources from noninvasive multichannel measurements of the magnetic field. Presumably, an

inverse procedure with anatomic constraints provided by imaging would yield a more accurate estimation of physiological biomagnetic sources, but computation of the SCD map does not require additional structural information or computationally expensive co-registration and/or inverse algorithms. In the past, our group and others have attempted to use a dipole fitting approach to track gastric biomagnetic sources [26;27]. This approach can present difficulties with solutions stuck in local minima and can be affected the initial estimate of the dipole location. It is possible that the SCD method could be used to provide an initial estimate for the dipole fitting approach or for other inverse procedures.

We have only used the z-components of the magnetic field since they are the components available to us in our measurements, and typically available in most existing biomagnetometer systems. But recent studies demonstrating the utility of full vector measurements have impelled the development of multichannel vector magnetometers, and our future work will investigate the further use of tangential components in estimating the SCD.

We have illustrated the application of the SCD method to evaluate gastric slow wave propagation, but the method could be applied in other biomagnetic recording situations as well. Knosche and colleagues used a method called Brain Surface Current Density (BSCD) mapping to compute activity on the cortical surface from extracranial magnetoencephalography measurements [28]. That technique is essentially an inward continuation of the external biomagnetic signals and requires an anatomical correlate from MRI, whereas the method presented here is a much more simplistic analysis of only the biomagnetic data. The BSCD method could be applied in our situation if anatomical imaging information were available as well.

The SCD method we used to analyze gastric propagation has been applied extensively in both adult and fetal magnetocardiography [29–35] as well as magnetoencephalography [36;37] and magnetoneurography [38], as noted by Haberkorn et al in their review [24]. They presented a model study of “pseudo current density maps” derived from H-C transformations and even propose the possibility of a hardware realization of the technique using novel sensor configurations [24]. Our results suggest that a planar implementation of a dense array of such sensors would allow direct assessment of the spatial gradient in gastric propagation velocity [1].

Acknowledgments

This work was supported in part by the National Institutes of Health under Grants DK58697 and DK64775.

The authors thank the SR Light Animal Laboratories at Vanderbilt University for technical assistance with animal surgery and Juliana Kim for assistance with the numerical simulations. We appreciate the helpful comments of the reviewers. This work is supported in part by NIH grants R01 DK 58197 and R01 DK 64775.

References

1. Sanders, KM.; Publicover, NG. Electrophysiology of the gastric musculature. In: Makhlouf, GM.; Schultz, SG., editors. Handbook of Physiology: The Gastrointestinal System. 1989. p. 187-216.
2. Kingma YJ. The electrogastrogram and its analysis. CRC Crit Rev Bioeng 1989;17(2):105–132.
3. Hamilton JW, Bellahsene BE, Cascio DE, Webster JG, Bass P. Human electrogastrograms: Comparison of techniques of recording. Am J Gastroenterol 1988;83(8):806–811. [PubMed: 3394684]
4. Alvarez WC, Mahoney LJ. Action Currents in Stomach and Intestine. Am J Physiol 1922;58(3):476–493.
5. Bradshaw LA, Ladipo JK, Staton DJ, Wikswo JP Jr, Richards WO. The human vector magnetogastrogram and magnetoenterogram. IEEE Trans Biomed Eng Aug;1999 46(8):959–970. [PubMed: 10431461]

6. Bradshaw LA, Allos SH, Wikswo JP Jr, Richards WO. Correlation and comparison of magnetic and electric detection of small intestinal electrical activity. Am J Physiol May;1997 272(5 Pt 1):G1159–G1167. [PubMed: 9176226]
7. Bradshaw LA, Myers AG, Redmond A, Wikswo JP, Richards WO. Biomagnetic detection of gastric electrical activity in normal and vagotomized rabbits. Neurogastroenterol Motil Oct;2003 15(5):475–482. [PubMed: 14507349]
8. Bradshaw LA, Richards WO, Wikswo JP Jr. Volume conductor effects on the spatial resolution of magnetic fields and electric potentials from gastrointestinal electrical activity. Med Biol Eng Comput Jan;2001 39(1):35–43. [PubMed: 11214271]
9. Chen JD, Zou X, Lin X, Ouyang S, Liang J. Detection of gastric slow wave propagation from the cutaneous electrogastrogram. Am J Physiol Aug;1999 277(2 Pt 1):G424–G430. [PubMed: 10444457]
10. Mintchev MP, Kingma YJ, Bowes KL. Accuracy of cutaneous recordings of gastric electrical activity. Gastroenterology May;1993 104(5):1273–1280. [PubMed: 8482441]
11. Geselowitz DB. On the magnetic field generated outside an inhomogeneous volume conductor b. IEEE Trans Magn 1970;MAG-6(2):346–347.
12. Sarvas J. Basic mathematical and electromagnetic concepts of the biomagnetic inverse. Phys Med Biol 1987;32(1):35390.
13. Pullan A, Cheng L, Yassi R, Buist M. Modelling gastrointestinal bioelectric activity. Progress in Biophysics and Molecular Biology 2004;85(2–3):523–550. [PubMed: 15142760]
14. Cheng LK, Komuro R, Austin TM, Buist ML, Pullan AJ. Anatomically realistic multiscale models of normal and abnormal gastrointestinal electrical activity. World J Gastroenterol Mar;2007 13(9): 1378–1383. [PubMed: 17457969]
15. Spitzer V, Ackerman MJ, Scherzinger AL, Whitlock D. The visible human male: a technical report. J Am Med Inform Assoc Mar;1996 3(2):118–130. [PubMed: 8653448]
16. Mirizzi N, Stella R, Scafoglieri U. Model to simulate the gastric electrical control and the response activity. Med & Biol Eng & Comput 1986;24:157–163. [PubMed: 3754916]
17. Mintchev MP, Bowes KL. Computer simulation of the impact of different dimensions of the stomach on. Med Biol Eng Comput 1998;36:7–10. [PubMed: 9614741]
18. Familoni BO, Abell TL, Bowes KL. A model of gastric electrical activity in health and disease. IEEE Trans Biomed Eng 1995;42(7):647–657. [PubMed: 7622148]
19. Bauer AJ, Publicover NG, Sanders KM. Origin and spread of slow waves in canine gastric antral circular muscle. Am J Physiol 1985;249:G800–G806. [PubMed: 4083358]
20. Cohen D, Hosaka H. Part II: magnetic field produced by a current dipole. J Electrocardiol 1976;9(4): 409–417. [PubMed: 978094]
21. Cohen D, Lepeschkin E, Hosaka H, Massell BF, Myers G. Part I: abnormal patterns and physiological variations in magnetocardiograms. J Electrocardiol 1976;9(4):398–409. [PubMed: 135816]
22. Hosaka H, Cohen D. Part IV: visual determination of generators of the magnetocardiogram. J Electrocardiol 1976;9(4):426–432. [PubMed: 978096]
23. Hosaka H, Cohen D, Cuffin BN, Horacek BM. Part III: the effect of the torso boundaries on the magnetocardiogram. J Electrocardiol 1976;9(4):418–425. [PubMed: 978095]
24. Haberkorn W, Steinhoff U, Burghoff M, Kosch O, Morguet A, Koch H. Pseudo current density maps of electrophysiological heart, nerve or brain function and their physical basis. Biomagn Res Technol 2006;4:5. [PubMed: 17040559]
25. Oostendorp TF, Vanoosterom A, Huiskamp G. Interpolation on A Triangulated 3D Surface. Journal of Computational Physics 1989;80(2):331–343.
26. Cheng LK, Buist ML, Richards WO, Bradshaw LA, Pullan AJ. Noninvasive localization of gastric electrical activity. Intl J Bioelectromagnetism 2005;7(1):1–4.
27. Allescher HD, Abraham-Fuchs K, Dunkel RE, Classen M. Biomagnetic 3-dimensional spatial and temporal characterization of electrical activity of human stomach. Dig Dis Sci 1998;43(4):683–693. [PubMed: 9558020]
28. Knosche TR, Maess B, Friederici AD. Processing of syntactic information monitored by brain surface current density mapping based on MEG. Brain Topogr 1999;12(2):75–87. [PubMed: 10642007]

29. Hailer B, Van LP, Chaikovsky I, uth-Eisernitz S, Schafer H, Gronemeyer D. The value of magnetocardiography in the course of coronary intervention. Ann Noninvasive Electrocardiol Apr; 2005 10(2):188–196. [PubMed: 15842431]

30. Koch H. Recent advances in magnetocardiography. J Electrocardiol 2004;37(Suppl):117–122. [PubMed: 15534820]

31. Hosono T, Shinto M, Chiba Y, Kandori A, Tsukada K. Prenatal diagnosis of fetal complete atrioventricular block with QT prolongation and alternating ventricular pacemakers using multi-channel magnetocardiography and current-arrow maps. Fetal Diagn Ther May;2002 17(3):173–176. [PubMed: 11914571]

32. Kandori A, Shimizu W, Yokokawa M, Noda T, Kamakura S, Miyatake K, Murakami M, Miyashita T, Ogata K, Tsukada K. Identifying patterns of spatial current dispersion that characterise and separate the Brugada syndrome and complete right-bundle branch block. Med Biol Eng Comput Mar; 2004 42(2):236–244. [PubMed: 15125155]

33. Kandori A, Miyashita T, Tsukada K, Hosono T, Miyashita S, Chiba Y, Horigome H, Shigemitsu S, Asaka M. Prenatal diagnosis of QT prolongation by fetal magnetocardiogram--use of QRS and T-wave current-arrow maps. Physiol Meas May;2001 22(2):377–387. [PubMed: 11411247]

34. Sato M, Terada Y, Mitsui T, Miyashita T, Kandori A, Tsukada K. Visualization of atrial excitation by magnetocardiogram. Int J Cardiovasc Imaging Aug;2002 18(4):305–312. [PubMed: 12123324]

35. Weber Dos SR, Kosch O, Steinhoff U, Bauer S, Trahms L, Koch H. MCG to ECG source differences: measurements and a two-dimensional computer model study. J Electrocardiol 2004;37(Suppl):123–127. [PubMed: 15534821]

36. Oe H, Kandori A, Murakami M, Miyashita K, Tsukada K, Naritomi H. Cortical functional abnormality assessed by auditory-evoked magnetic fields and therapeutic approach in patients with chronic dizziness. Brain Res Dec;2002 957(2):373–381. [PubMed: 12445982]

37. Kandori A, Oe H, Miyashita K, Date H, Yamada N, Naritomi H, Chiba Y, Murakami M, Miyashita T, Tsukada K. Visualisation method of spatial interictal discharges in temporal epilepsy patients using magneto-encephalogram. Med Biol Eng Comput May;2002 40(3):327–331. [PubMed: 12195980]

38. Burghoff M, Mackert BM, Haberkorn W. Visualization of action currents in peripheral nerves from the biomagnetic field. Biomed Tech 2005;50:179–180.

Biographies

L. Alan Bradshaw was born in Carbondale, IL in 1968. He received the BS degree in physics from Abilene Christian University, Abilene, TX, in 1990, and the MS and PhD degrees in physics, both from Vanderbilt University, Nashville, TN in 1992 and 1995, respectively. He received a National Research Service Award from the National Institutes of Health in 1996 to work on biomagnetic measurements of intestinal electrical activity and became the first Director of the Gastrointestinal Superconducting QUantum Interference Device (SQUID) Technology Laboratory at Vanderbilt. In 1998, he joined the faculty of Lipscomb University as an Assistant Professor while continuing to maintain joint appointments at Vanderbilt as Research Assistant Professor in the Department of Physics and Astronomy and in the Department of Surgery. His research interests include biomagnetic and bioelectric detection of gastrointestinal electrical activity and the application of biomagnetic methods to diagnosis of gastrointestinal disorders. In 2006, Dr. Bradshaw and his collaborators were awarded the Nightingale Prize for the Best Paper of 2005 in Medical & Biological Engineering & Computing. His teaching interests are in undergraduate science general education, premedical physics education, and the intersection of science and religion. His wife Leah is a registered nurse and they have three children: Zach, Katherine and Lindsay.

Leo K. Cheng received the B.E. (Hons) degree in Engineering Science and the Ph.D. degree in Bioengineering both from The University of Auckland, New Zealand, in 1997 and 2001, respectively. He is currently a Senior Research Fellow at the Auckland Bioengineering Institute, The University of Auckland. His research interests include using bioelectromagnetic recordings along with mathematical and computational modeling techniques to improve the understanding of physiological function and to aid clinical diagnosis.

William Richards received the MD degree from the University of Maryland, Baltimore. After finishing his residency in general surgery in 1984, he completed a research fellowship in GI physiology at Vanderbilt University in 1987. He is currently Ingram Professor of Surgical Sciences at Vanderbilt University School of Medicine. His current research interests include the electrophysiology of gastrointestinal smooth muscle.

Andrew Pullan received his BSc (Hons) in Mathematics in 1985 and his PhD in Engineering in 1988, both from the University of Auckland. He joined the Department of Engineering Science at the University of Auckland in 1989, and is currently Professor and Head of the Department. He is also a principal investigator in the Auckland Bioengineering Institute and an Adjunct Associate Professor in the Department of Surgery at Vanderbilt University. Much of his research focuses on the electrical activity of the various muscles (cardiac, smooth and skeletal) of the human body. His work has a particular emphasis on detailed biophysically based modeling and the connection between the modeling and clinical domains.

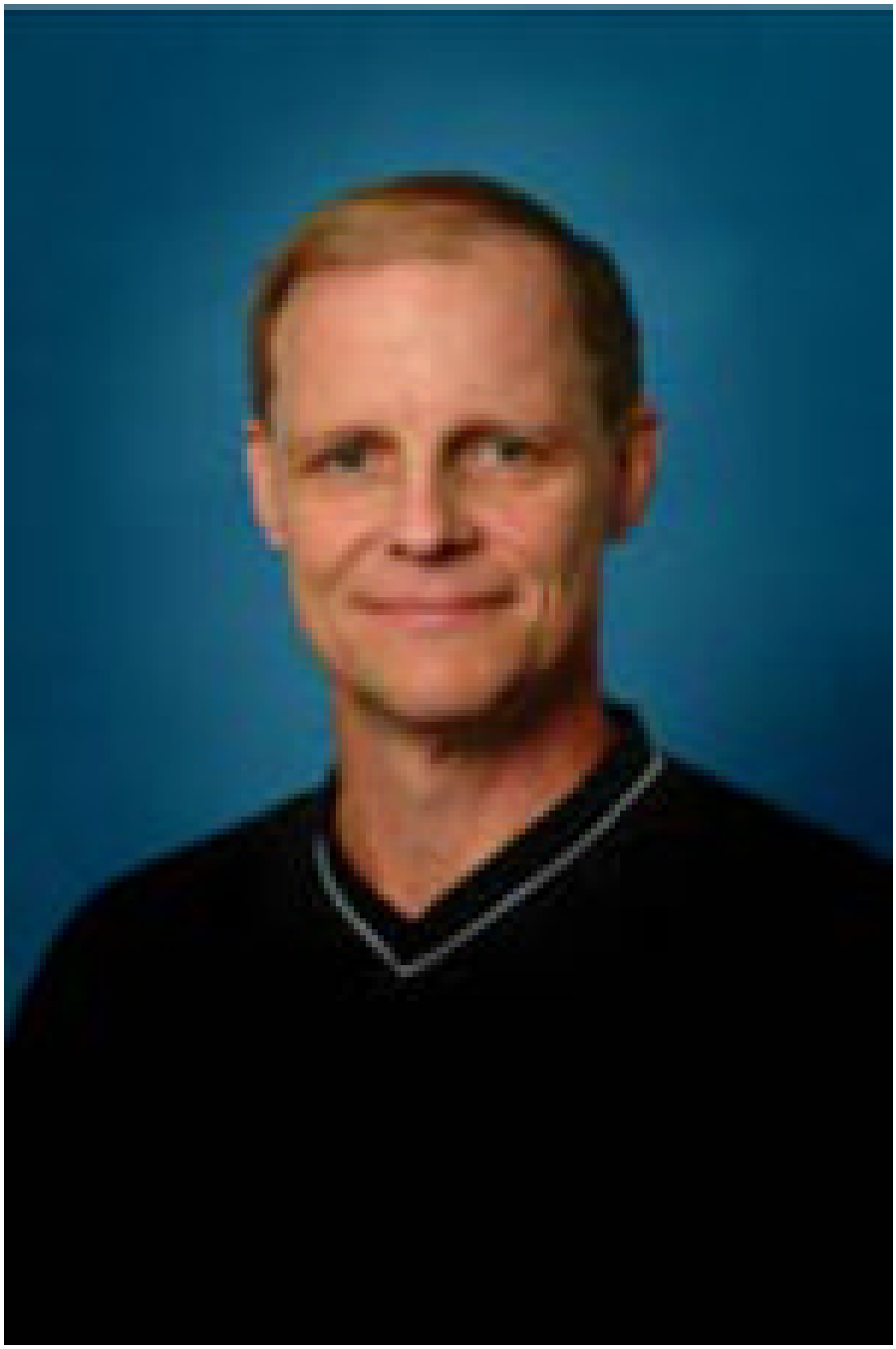

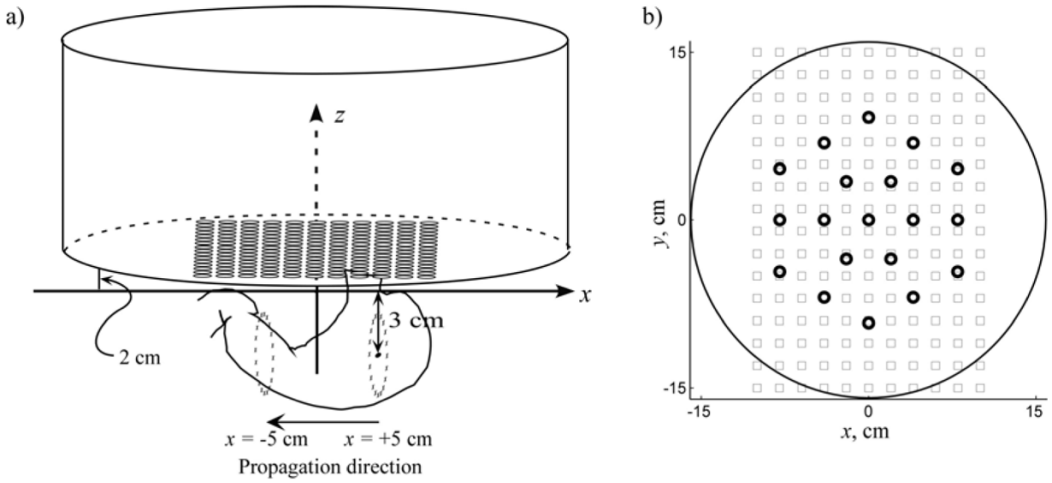

Figure 1.

(a) The dipole ring propagates longitudinally down the stomach beneath the magnetometer. (b) Sensor positions are shown as squares for the hypothetical high-density 176 channel magnetometer arranged in a 16×11 rectangular array and as circles for the Tristan 637i biomagnetometer in use at Vanderbilt.

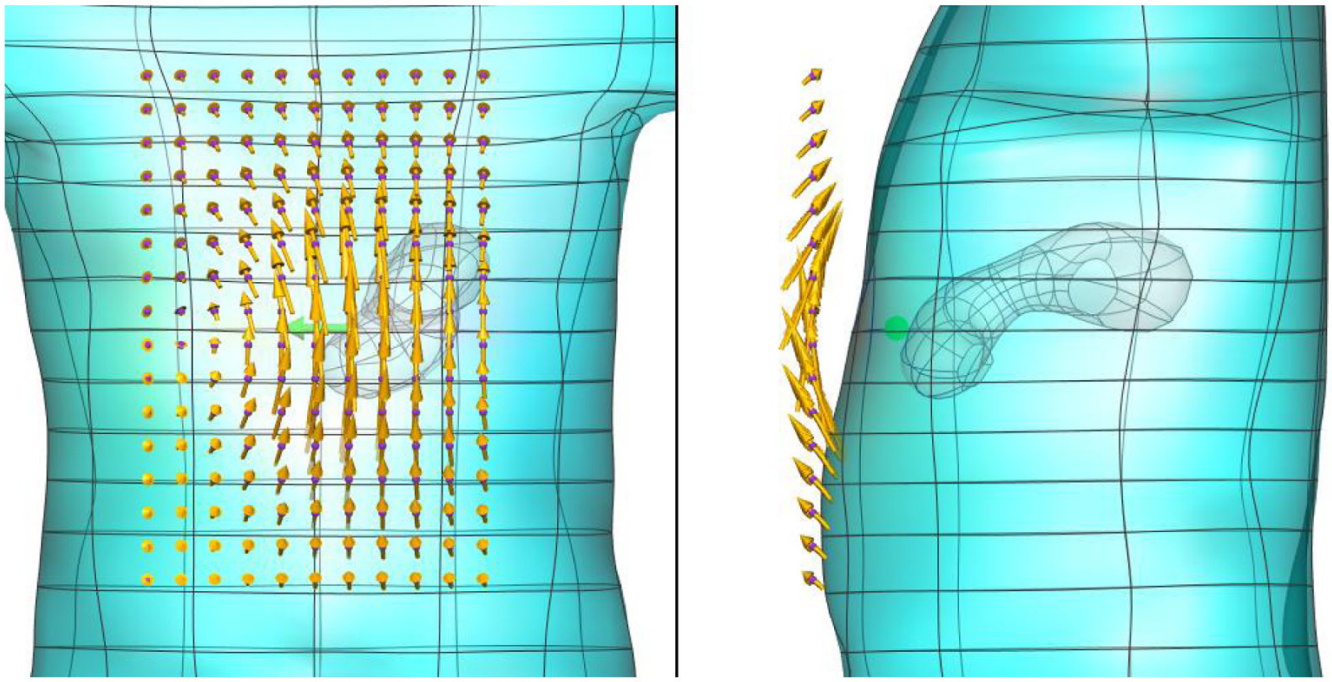

Figure 2.
In the realistic-abdomen volume conductor, recorded magnetic fields are represented by arrows located at the sensor positions. The current dipole is represented by the arrow underneath the skin surface. For this simplistic simulation, the dipole propagated in a straight line from the subject's left to right across the abdomen and was not constrained to the surface of the stomach.

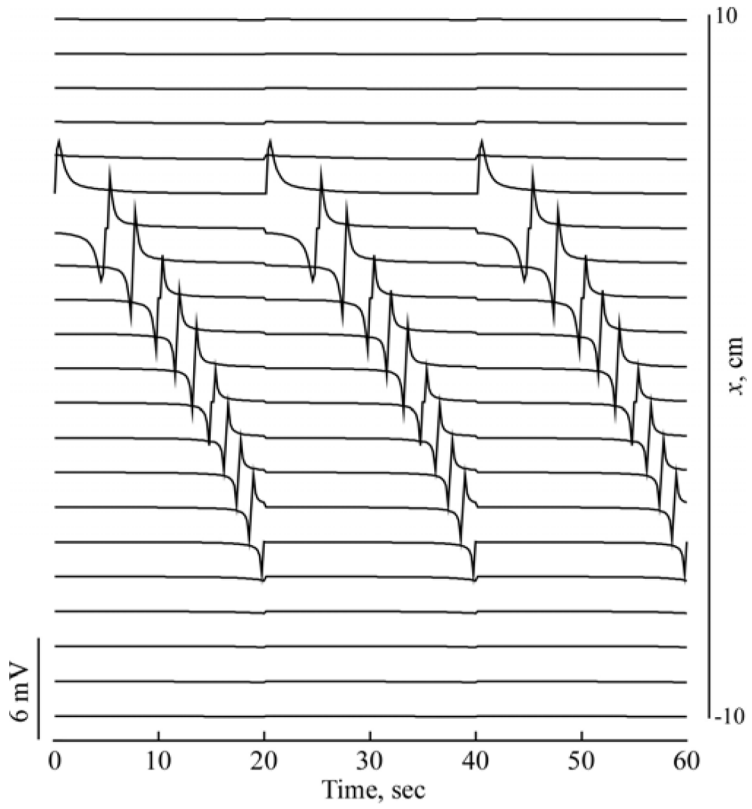

Figure 3.
Serosal potential waveforms computed from homogeneous half-space model exhibit propagating activity.

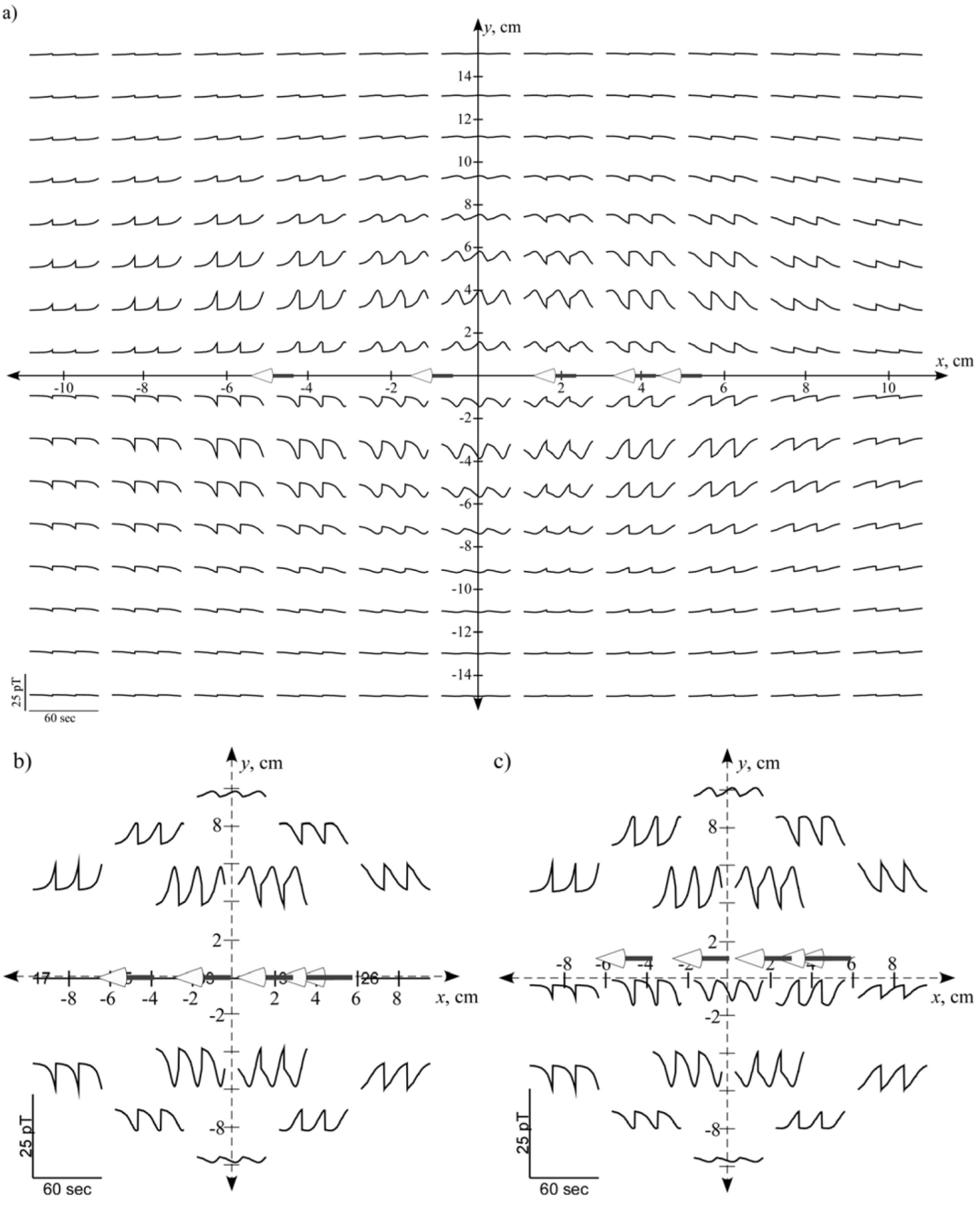

Figure 4.

(a) Magnetic induction field in a 176 channel magnetometer from a ring of dipoles (represented by arrows) propagating with increasing velocity along $y = 0$ from $x = +5$ to $x = -5$ in a homogeneous layered half-space. (b) Magnetic fields in the Tristan 637i magnetometer array computed from the same propagating source as in (a). (c) The same source and detectors as in (b), but with the source propagation along $y = 1$ cm instead of $y = 0$ cm.

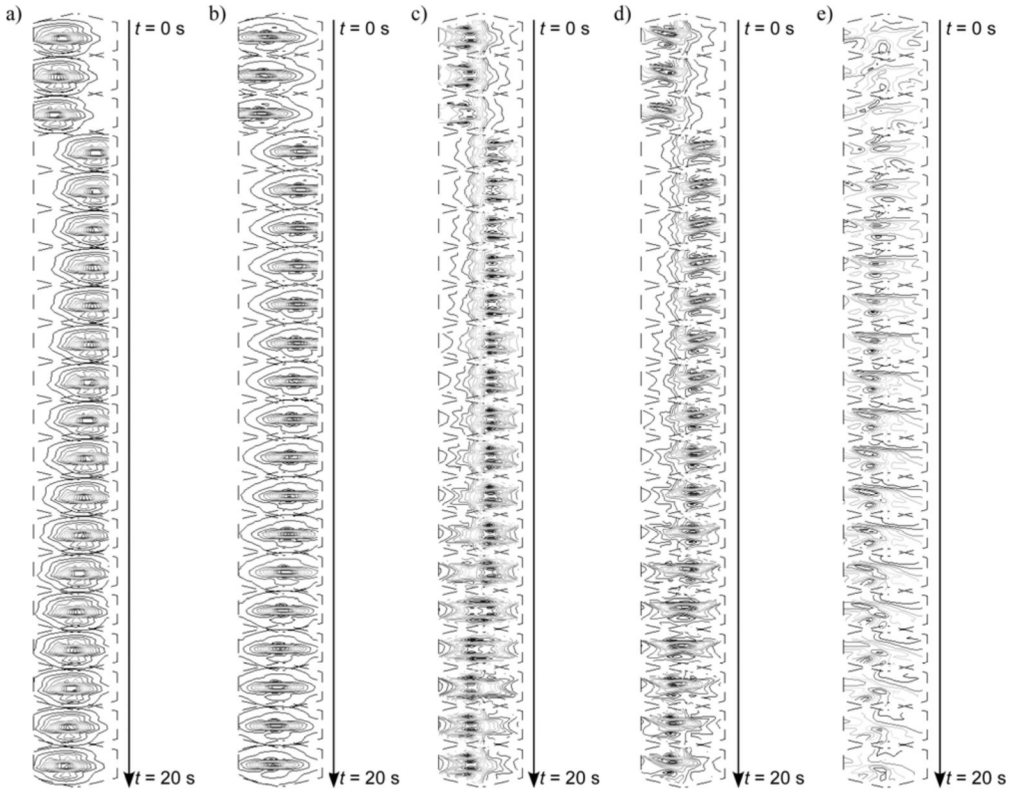

Figure 5.

SCD sequences of magnetic field data from (a) the volume conducting half-space model with the high-density (176 channel) magnetometer, (b) the realistic volume conductor model using the high-density magnetometer, (c) the volume-conducting half space model with the Tristan 637i array, (d) same as in (c) but with the propagation pattern not directly underneath the central sensors in the array, (e) experimental data. The lower spatial resolution in (c) and (d) makes the propagating maximum appear to jump between sensor positions.

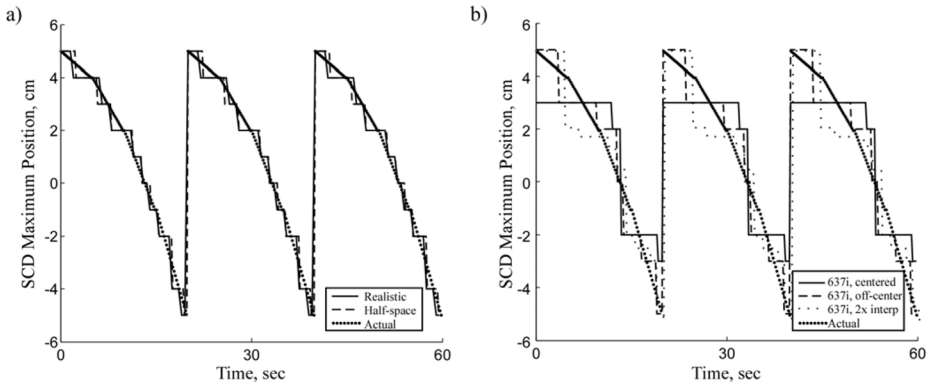

Figure 6.

The position of the SCD maximum as a function of time allows computation of the propagation velocity. (a) The SCD maxima for the high density sensors in the case of the realistic volume conductor and conducting half-space are very similar and both are close to the actual dipole positions. (b) The lower spatial sampling of the Tristan 673i obscures details about the dipole propagation, particularly if the propagation occurs directly underneath the sensors. Doubling the interpolation of the magnetic field provides a modest increase in the accuracy of the dipole position estimate provided by SCD.

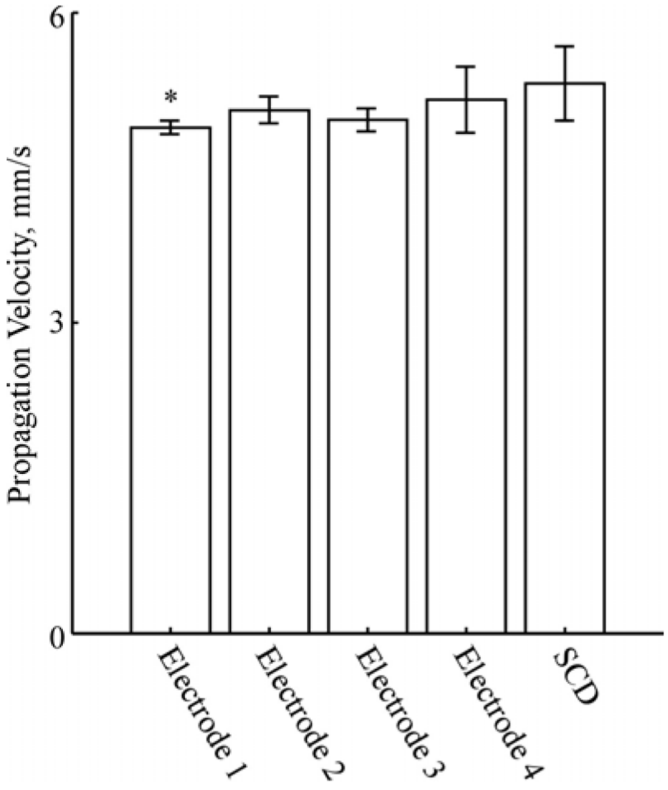

Figure 7.
Propagation velocity as measured in four bipolar serosal electrodes in a porcine experiment agrees with the propagation velocity determined by applying the SCD to noninvasive SQUID measurements using the Tristan 637i. Only the propagation velocity determined from the first, most proximal, serosal electrode pair was significantly different from the velocity obtained by SCD mapping.